ARTICLE

Improving long-term electrochemical performances of Li-rich cathode material via encapsulating three-in-one nanolayer

Zhenbo Wang,[a] Yanfeng Yin,[a,b] Guanjie He,[c] Huiling Zhao*[a,b] and Ying Bai*[a,b]

ABSTRACT: With large specific capacity, wide voltage window, and high energy density, Li-rich layered oxides have been considered as one promising cathode candidate for advanced lithium-ion batteries (LIBs). However, their commercial application is in dilemma due to severe capacity degradation and voltage fading caused by irreversible oxygen evolution and phase transition happened upon repeated cycling. This work proposes an effective strategy to improve long-term electrochemical performances of $Li_{1.2}Mn_{0.56}Ni_{0.17}Co_{0.07}O_2$ (LMNCO) through constructing multifunctional nanolayer composed of element-doping, layered-spinel heterostructural connection, and fast ion conductor shell via a facile method. $Li_{0.09}B_{0.97}PO_4$ (LBPO) coating shell acts as fast ion carrier and physical screen to promote Li^+ diffusion and isolate side reactions at cathode-electrolyte interface, meanwhile two-phase transitional region provides three-dimensional channel to facilitate Li^+ transport and inhibit phase transition, besides B^{3+} and PO_4^{3-}-doping collaborates with oxygen vacancy to stabilize lattice oxygen and restrain oxygen evolution from bulk active cathode. The optimized LMNCO@LBPO material exhibits a superior capacity retention of 78.6%, higher than pristine sample (49.3%), with the mitigated voltage fading of 0.73 mV per cycle after 500 cycles at 1 C. This study opens up an avenue for the surface modification to the electrochemical properties and perspective application of Li-rich cathodes in high-performance LIBs.

Introduction

The growing market of mobile electric vehicles has promoted the rapid development of high-energy-density lithium-ion batteries (LIBs).[1–4] Li-rich layered oxides with the chemical formula of $xLi_2MnO_3 \cdot (1-x)LiMO_2$ (M = Ni, Co, Mn, etc.), possessing extraordinary specific capacity (> 250 mAh g^{-1}), wide voltage window (2.0–4.8 V vs. Li/Li^+), and high energy density (~103 Wh kg^{-1}), have spurred extensive attention in the current research of high-performance LIBs field.[5–7] And it has been demonstrated that the exceptional specific capacity of Li-rich material is associated with the cumulative redox reaction of cations and anions when cycled above 4.5 V.[8] However, the practical application of Li-rich cathodes is in dilemma because severe electrochemical issues such as low initial coulombic efficiency (ICE), poor electrode kinetics, and serious voltage fading inevitably happen at high-voltage charging-discharging processes.[9,10] Under high charge cut-off voltage, typically in the range of 4.5–4.8 V, more Li^+ ions are delithiated from Li-rich cathode, more transition metal (TM) ions will migrate from TM sites to neighbouring Li^+ vacancies, easily triggering layered-to-spinel phase transition, TM dissolution, and oxygen extraction occurred.[11,12] In subsequence, TM dissolution

and oxygen release at high operation voltages tend to exacerbate side reactions and abet the growth of improper solid-electrolyte interphase (SEI) layer at cathode-electrolyte interface (CEI), leading to rapid increase of interface impedance, depressed Li^+ diffusion, continuous capacity degradation and voltage fading in repeated cycles.[13–15]

To ameliorate aforementioned issues, various surface treatments from physical and chemical aspects have been carried out to enhance the long-term cyclability of Li-rich materials.[16] The design of interfacial layer should satisfy following features: (1) displays physical barrier separating Li-rich cathode from liquid electrolytes to depress the dissolution of TM elements and the attack of HF acid, thus reducing SEI growth and electrolyte decomposition; (2) suppresses Jahn-Teller effect and irreversible phase transition, maintaining structural stability and depressing oxygen loss in long-term cycling; (3) facilitates Li^+ ions diffusion at CEI, enhancing the kinetics and rate performance of Li-rich cathode. Nowadays, compounds such as inorganic oxides (Al_2O_3, ZnO, TiO_2),[17–19] phosphates ($AlPO_4$, $Li_3V_2(PO_4)_3$, $LiMnPO_4$),[20-22] fluorides (MgF_2, AlF_3, LaF_3),[23–25] lithium-ion conductor ($LiVO_3$, $Li_4Ti_5O_{12}$, $LiSnO_2$, $LiAlF_4$),[26–29] and organic dual-conductive polymers,[30] have been utilized as coating materials to promote the electrochemical performances of Li-rich cathodes. In these studies, it has been verified that the formation of spinel-phase interlayer can suppress the loss of lattice oxygen and enhance the anionic redox reactions during electrochemical process.[27] The introduce of oxygen vacancies in surface region can strengthen the phase compatibility between coating layer and bulk active material, but also effectively suppresses voltage decay and capacity degradation of Li-rich cathode in cycling.[31] In our previous research, one-step integrated surface

[a]International Joint Research Laboratory of New Energy Materials and Devices of Henan Province, School of Physics and Electronics, Henan University, Kaifeng, 475004, ChinaAddress here.
[b]Academy for Advanced Interdisciplinary Studies, Henan University, Kaifeng, 475004, China.
[c]Materials Research Center, UCL Department of Chemistry, Christopher Ingold Building, 20 Gordon Street, London, WC1H, 0AJ, UK
Corresponding author. E-mail: zhao@henu.edu.cn; ybai@henu.edu.cn

modification involving vanadium (V)-doping and $Li_3V_2(PO_4)_3$ coating has been explored to harvest the optimized interface properties and the promoted electrochemical performances of high-voltage cathode.[32]

In this work, a synchronous engineering strategy of three-in-one nanolayer composed of element-doping, layered-spinel heterostructural transition region, and fast ion conductor shell is proposed (Fig. 1a) for the surface modification of Li-rich cathode. $Li_{0.09}B_{0.97}PO_4$ (LBPO), one mineral adhesive compound with high Li^+ diffusion coefficient of 3.35×10^{-5} S cm^{-1},[33] is deliberately selected as coating material, acting as physical screen onto layered oxide $Li_{1.2}Mn_{0.56}Ni_{0.17}Co_{0.07}O_2$ (LMNCO) against detrimental interfacial electrode/electrolyte reactions and TM dissolution, besides introducing trivalent bromide (B^{3+}) and polyanion (PO_4^{3-})-doping to stabilize lattice oxygen and restrain oxygen evolution of Li-rich cathode in cycling. Additionally, the synchronously-produced transitional region with two-phase heterostructure can enhance the compatibility of LBPO coating and bulk LMNCO active material, as well as facilitate Li^+ transport and depress phase transition of Li-rich cathode. Various characterization techniques have been employed to comprehensively investigate the microstructure evolution and electrochemical performance of as-synthesized materials. It is manifested that the rate performance, cycle stability and average discharge voltage of LMNCO cathode can be effectively improved through LBPO modification, e.g., the superior capacity retention of 78.6%, higher than pristine sample (only 49.3%), and the mitigated voltage fading of 0.73 mV per cycle after 500 cycles at 1 C.

Experimental

Material synthesis

The pristine LMNCO sample was synthesized by using a conventional sol-gel method. Briefly speaking, metal acetates including $CH_3COOLi \cdot 2H_2O$ (Kermel), $Mn(CH_3COO)_2 \cdot 4H_2O$ (Aladdin), $Co(CH_3COO)_2 \cdot 4H_2O$ (Aladdin), and $Ni(CH_3COO)_2 \cdot 4H_2O$ (Aladdin) were separately dissolved into ethyl alcohol at room temperature, then the acquired solutions were dropped into the citric acid (Kermel) solution (with metal cations: $C_6H_8O_7$ = 1:1) under vigorous stirring. The mixed solution was evaporated at 80 °C until a light purpled sol formed, which was afterward dried at 120 °C for 12 h to acquire the corresponding gel. Subsequently, the gel was ground adequately and calcined at 450 °C for 10 h to remove organic contents, further annealed again at 900 °C for 12 h to obtain the pristine LMNCO sample.

LBPO-modified LMNCO (LMNCO@LBPO) samples including LMNCO@1%LBPO, LMNCO@2%LBPO, and LMNCO@3%LBPO, were prepared with different weight percentages of LBPO coating (1, 2, 3 wt.%) through a conventional sol-gel method. Firstly, the stoichiometric amount of $NH_4H_2PO_4$ (AR, Kermel) and H_3BO_3 (99.9%, Aladdin) were together dissolved into distilled water at 90 °C under strong stirring, and then a certain amount of $LiOH \cdot H_2O$ (99.0%, Aladdin) was slowly added to form a transparent solution. Secondly, the as-prepared pristine LMNCO powder was dispersed into distilled water, and the above-obtained LBPO precursor solution was added dropwise with vigorous stirring. The mixed solution was evaporated at 90 °C and dried at 100 °C to acquire a xerogel product. Finally, the gel was ground adequately and heated in air at 110 °C for 2 h, subsequently annealed at 500 °C for 6 h to obtain the LBPO-modified samples with different LBPO contents.

Materials characterization

Crystal structures of all the as-synthesized materials were characterized by X-ray diffraction (XRD, Bruker D8 Advance, Germany) recorded in the range of 10–80° with a scanning rate of 0.03° s^{-1}. Raman spectra (Renishaw RM-1000, 633 nm He-Ne laser) were collected to investigate the composition and microstructure information of all samples. Morphologies and microstructures of all as-synthesized materials were observed by field emission scanning electron microscopy (FESEM, JEOL 7001F, Japan) and high-resolution transmission electron microscopy (HRTEM, FEI Tecnai G2 F20), meanwhile elemental distributions were detected by energy dispersive spectroscopy (EDS) and fast Fourier transform of HRTEM image for the selected region was also carried out by Digital Microscopy software. Chemical environments of all as-prepared samples were analyzed by X-ray photoelectron spectroscope (XPS, ESCALAB 250Xi, Thermo Fisher Scientific, America) with Al Kα radiation (150 W, 1486.6 eV). Additionally, in-depth XPS profiles were collected on the spectrometer instrument (PHI 5000 Versa Probe-II, Japan) with Al Kα radiation (50 W, 15 kV) at a pressure of 10^{-8} Torr, in which argon (Ar)-ion beam with the density of 25 μA mm^{-2} and accelerating voltage of 2.0 kV was employed in etching process. Inductively coupled plasma (ICP) analysis was conducted on Thermo Fisher ICAP 6300 to determine the accurate concentration of several elements dissolved into electrolyte from the as-synthesized samples.

Electrochemical measurements

The powder of as-prepared material (as active cathode material), acetylene black (as conductive agent) and polyvinylidene fluoride (as binder) were mixed with a weight ratio of 8:1:1 and ground thoroughly, followed by dissolving in N-methyl-2-pyrrolidone to form a homogeneous slurry. Next, the mixed slurry was uniformly spread onto a piece of aluminum foil, and dried at 100 °C for 12 h. The dried foil was cut into square sheets as electrodes with a size of 8 mm × 8 mm, and the coin cells (CR2032) were assembled in an argon-filled glove box, using Li foil as counter electrodes and Calgary 2400 porous polypropylene film as separators. The mass loading of active material for electrode was ~2.6 mg cm^{-2}. The used electrolyte was composed of 1 M $LiPF_6$ in ethylene carbonate and dimethyl carbonate with the volume ratio of 1:1. Electrochemical performances of all the assembled LMNCO|Li or LMNCO@LBPO|Li half cells (CR2032-type) were evaluated via LAND CT2001 A (Wuhan, China) test instrument in the voltage range of 2.0–4.8 V. Cyclic voltammetry (CV) test at different scan rates and electrochemical impedance spectroscopy (EIS) measurement at the charged state of 4.8 V with an amplitude of 5 mV in the frequency range over 10^{-2}–10^5 Hz were accomplished on an electrochemical workstation (CHI660E, Shanghai Chenhua).

Aging analysis

Before aging experiment, as-prepared cathode materials are thoroughly dried to avoid any possible influence from the adsorbed water. Then, 0.4 g powders of pristine LMNCO and LMNCO@2%LBPO samples were respectively dispersed into 50 mL electrolytes and

packed into polytetrafluoroethylene (PTFE) containers, which were carefully sealed and aged at 50 °C with magnetic stirring. After specific time periods (1, 2, and 3 weeks), 10 mL solution was drawn out and followed by liquid-solid separation for the subsequent ICP test to measure the contents of nickel (Ni), cobalt (Co) and manganese (Mn) elements dissolved into electrolyte from as-synthesized samples.

Results and discussion

XRD patterns of all the as-synthesized materials are shown in Fig. 1b, wherein main diffraction peaks can be indexed to hexagonal $LiMO_2$ structure with $R\bar{3}m$ space group, besides monoclinic Li_2MnO_3 phase (C/2m) appeared around 20°–23°.[34] Clear splittings of (006)/(102) and (018)/(110) peaks indicate the highly-ordered layered structure possessed by all samples.[35] There is no obvious diffraction peak of LBPO composite observed due to its small amount of coating content, whereas Fig. S1† demonstrates that the well-crystallized

LBPO material can be synthesized under the same experimental condition. Meticulous investigations on the enlarged graphs of (003) and (104) peaks, reveal that position shift and peak asymmetry happened to LBPO-modified samples. The peak position of LMNCO@LBPO sample is clearly shifted to a small angle with respect to the pristine LMNCO, indicating the enlargement of lattice parameters for LBPO-modified Li-rich cathode materials. Additionally, shoulder peaks marked with asterisk (∗) can be observed in the enlarged patterns of LMNCO@LBPO samples, which belong to the spinel phase ($Fd\bar{3}m$) of Li-rich material and their intensity became stronger with the higher coating content of LBPO.[36] To obtain more comprehensive crystallographic information, Rietveld refinement of XRD spectrum was carried out and the obtained results are shown in Fig. S2† with relevant calculated factors listed in Table S1.† It is manifested that the lattice *c*-parameter of LMNCO@2%LBPO sample is larger than that of pristine LMNCO, consistent with the (003) and (104) peaks shifted to small diffraction angle. More interestingly, a small percentage (2.7%) of
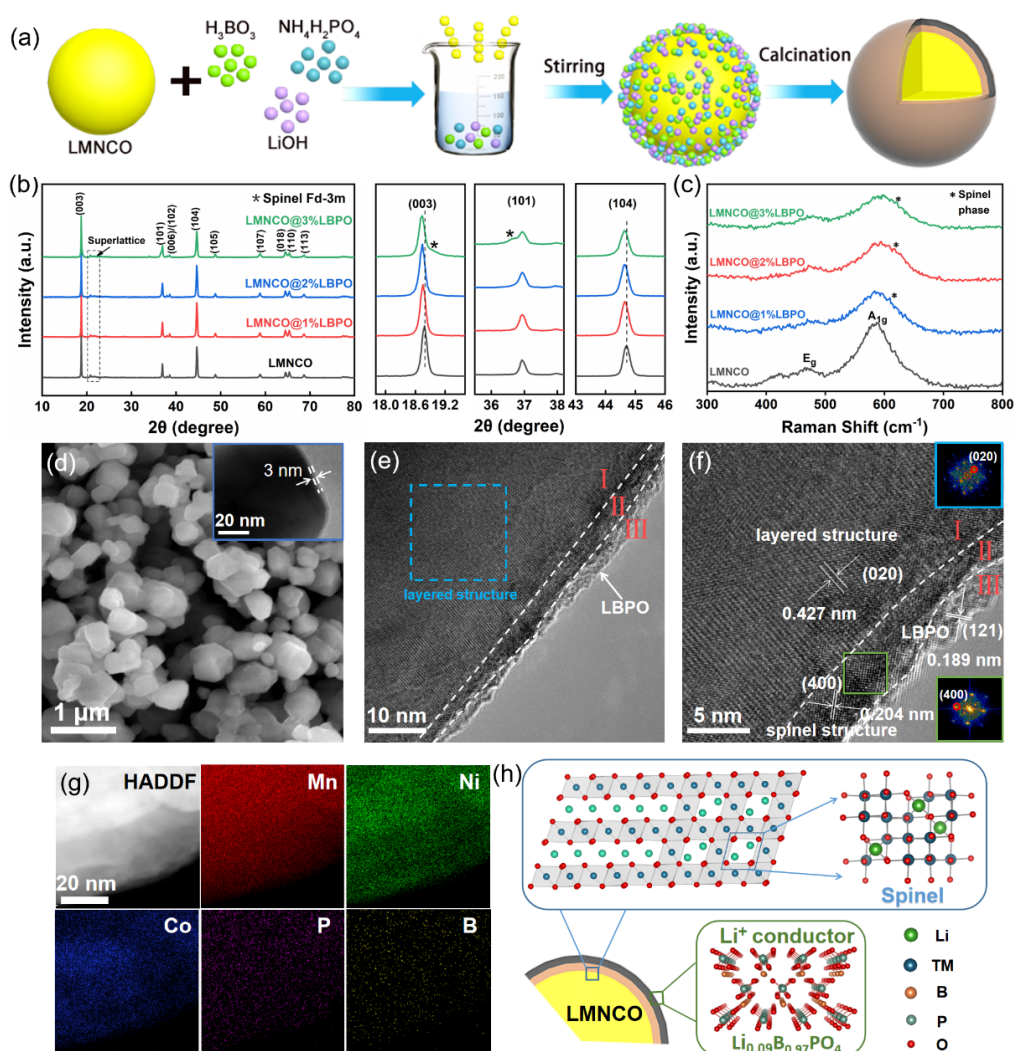

Fig. 1 (a) Schematic diagram of the synthesis process of the LBPO-modified LMNCO (LMNCO@LBPO) materials. (b) XRD patterns of all the as-synthesized materials. (c) Raman profiles of the as-prepared Li-rich cathode oxides. (d) SEM and TEM images of the LMNCO@2%LBPO sample. (e)(f) HRTEM images of the LMNCO@2%LBPO sample. (g) TEM image and elemental mappings (Mn, Ni, Co, P, and B) for the LMNCO@LBPO sample. (h) Schematic illustration for the crystal structures of three-in-one coating layer formed on the surface of bulk layered-structure LMNCO particle.

spinel phase ($\mathbf{Fd\bar{3}m}$) in Li-rich material can be recognized according to the refinement result of LMNCO@2%LBPO sample, indicating the spinel structure synchronously generated in LBPO modification.

Raman spectroscopy is an effective technique to distinguish different crystal phases embraced in surface region of the targeted material. All the as-synthesized samples have similar characteristics in Raman spectra (Fig. 1c) with three main peaks located around 432, 476, and 592 cm^{-1}, respectively. Usually, the peak at ~432 cm^{-1} is assigned to the phonon vibration of monoclinic Li$_2$MnO$_3$ structure contained in layered Li-rich oxides.[37] Two peaks near 476 and 592 cm^{-1}, are usually belonged to E$_g$ (O–TM–O bending mode) and A$_{1g}$ (TM–O stretching mode) vibrations of $\mathbf{R\bar{3}m}$ layered structure.[23] However, obvious broadening and blue shift of A$_{1g}$ peak are both observed, which are often caused by bond contraction and internal stress from the spinel-phase surface coating. Therefore, it is insinuated that spinel structure might be induced in the surface region of LBPO-modified samples, and the detailed microstructure of LMNCO@LBPO sample will be visualized using high-resolution transmission electron microscope (HRTEM) in following characterization.

Field emission scanning electron microscopy (FESEM) images (Fig. 1d and Fig. S3†) of all as-synthesized materials demonstrate the sizes and morphologies of LBPO-modified particles have no obvious change compared with pristine LMNCO, possessing smooth shape and even size distribution. However, TEM image (inset of Fig. 1d) indicates there existed uniform coating layer with the thickness of ~3 nm on the LMNCO@2%LBPO particle surface. To identify the subtle microstructure of LBPO-modified material, HRTEM characterization was conducted on LMNCO@2%LBPO sample. Fig. 1e exhibits there are two distinguishing regions roughly belonged to LMNCO core and LBPO shell, further a transitional connection with thickness of ~4 nm can be divided out referring to the crystalline analysis of these magnified regions. In Fig. 1f, the lattice fringes with interplanar distance of ~0.189 nm are assigned to (121) planes of LBPO compound marked in outer region, and the distance of ~0.427 nm can be attributed to (020) crystal planes of inner layered-structure

LMNCO material. Additionally, the interplanar spacing of those lattice fringes is measured to be 0.204 nm which should be indexed to (400) planes of the spinel-structured LMNCO with $\mathbf{Fd\bar{3}m}$ space group. Fourier transform (FT) analysis of the selected regions in TEM images (insets of Fig. 1f), further confirm these lattice fringes can be referred to the layered and spinel phases of Li-rich active material, respectively. That is, layered-spinel transitional region with two-phase heterostructure was synchronously produced during LBPO coating treatment, which has been implied in abovementioned XRD and Raman results. Furthermore, elemental mappings (Fig. 1g) of LMNCO@2%LBPO sample present that P and B elements are uniformly distributed on particle surface, indicating the existence of LBPO coating layer. As schemed in Fig. 1h, a novel surface modification composed of layered-spinel heterostructural connection and fast ion conductor LBPO outer shell is constructed onto bulk LMNCO particle surface, and the former will benefit the structure compatibility between inner Li-rich active material and outer LBPO coating shell, simultaneously the latter will resist the corrosion of electrolyte and promote Li$^+$ diffusion at CEI.

Oxidation and valence states of TM ions play vital roles in the crystalline structure and electrochemical performances of Li-rich cathode, herein surface chemical environment of as-synthesized material was investigated by XPS technique. All survey spectra have been calibrated by C$_{1s}$ for the pristine LMNCO and LMNCO@2%LBPO samples (Fig. 2a), in which signals of P and B elements appeared in the curve of LBPO-modified sample, except Co, Ni, Mn, and O elements in bulk LMNCO material. The peaks with binding energies (BEs) of 780.18 and 795.40 eV (Fig. S4a†) assigned to Co 2p$_{3/2}$ and Co 2p$_{1/2}$, respectively, indicate Co^{3+} contained in the as-synthesized samples.[38] As for Ni element (Fig. S4b†), Ni 2p$_{3/2}$ peaks with BEs of 854.54 and 855.64 eV should be assigned to Ni^{3+} and Ni^{2+}, respectively.[39] The higher content ratio of Ni^{3+}/Ni^{2+} in LMNCO@2%LBPO sample, indicates the lower degree of Li$^+$/Ni^{2+} mixing and the superior structural stability of the LBPO-modified sample.[40] Comparing Mn 2p spectra of the pristine LMNCO and LMNCO@2%LBPO samples (Fig. S4c†), the peaks at ~642.7 and 654.2
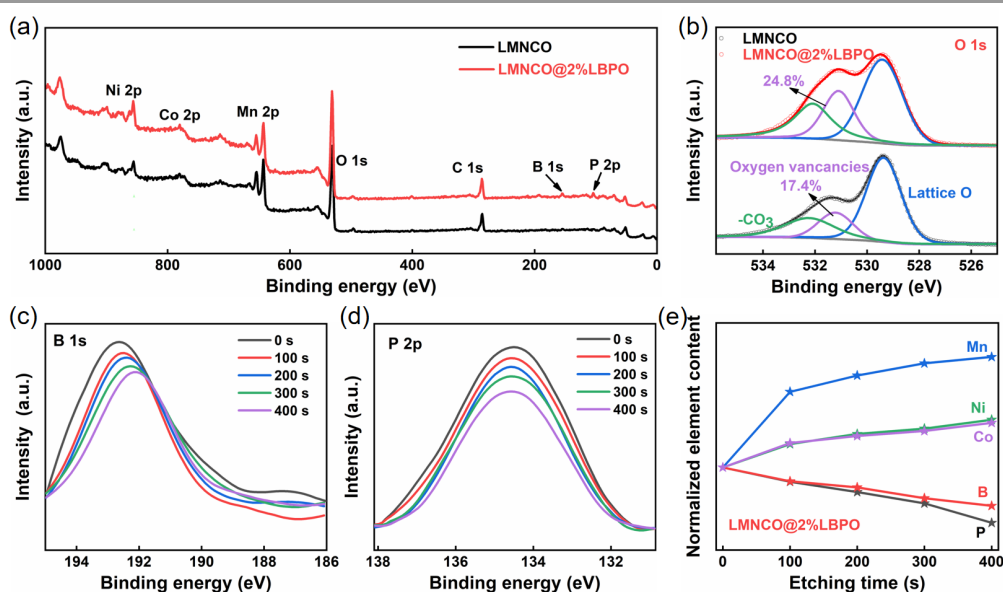

Fig. 2 (a) Survey XPS spectra and (b) O 1s of the LMNCO and LMNCO@2%LBPO samples. In-depth XPS profiles of (c) B 1s and (d) P 2p detected in the LMNCO@2% LBPO sample. (e) Normalized contents of Mn, Ni, Co, B, and P elements in the LMNCO@2%LBPO sample with increased etching time.

eV are coincided to Mn $2p_{3/2}$ and Mn $2p_{1/2}$ spin states, respectively, furthermore Mn $2p_{3/2}$ peak can be fitted into two peaks belonged to Mn^{3+} (641.6 eV) and Mn^{4+} (642.7 eV).[41] Valence state of Mn ion plays an important role in the crystalline structures and electrochemical performances of Mn-based oxide materials, since the Jahn-Teller distortion effect of Mn^{3+} usually induces more prominent irreversible phase transition and element dissolution of Li-rich cathodes upon repeated cycling.[42-44] Due to the formation of spinel phase and the increased Mn^{4+} content, it is indicated that the Jahn-Teller effect might be suppressed in the LMNCO@LBPO sample.[38]

As for O 1s spectra of these two samples (Fig. 2b), the integral area ratio of peak at 531.2 eV became higher from 17.4% to 24.8% before and after LBPO modification, suggesting the increase of oxygen vacancies during surface treatment. It has been widely acknowledged that some amount of oxygen vacancies in surface region could effectively facilitate Li^+ diffusion through activating lithium ions at tetrahedral sites and suppress the irreversible oxygen release from surface, thereupon to promote the electrochemical performance of Li-rich cathode.[45] In XPS spectra of LMNCO@2%LBPO sample, B 1s peak with BE of 192.44 eV (Fig. S4d†) assigned to B–O bond and P 2p peak at 134.05 eV (Fig. S4e†) ascribed to P–O bond were clearly detected, which confirmedly verifies the successful coating of LBPO material.[40] In addition, it has been reported that B^{3+} and PO_4^{3-} polyanion-doping easily happened in the surface modification of borate and phosphate salts,[46] thus in-depth XPS analysis was performed on the LMNCO@2%LBPO sample. XPS depth profiles (Fig. 2c,d and Fig. S4f–h†) were collected with an etching gap of 100 s per strip, and the signals of B, P, Mn, Ni, and Co elements were recorded. The normalized intensities (Fig. 2e) of B 1s and P 2p both decreased along with etching depth, inverse to the gradually-

growing intensities of Mn 2p, Ni 2p, and Co 2p signals, indicates that B^{3+} and PO_4^{3-} ions should be gradiently migrated into the surface of bulk LMNCO lattice. It has been reported that B^{3+} and PO_4^{3-} ions tend to occupy tetrahedral interstitial sites surrounded by three planes of MO_6 octahedra and one plane of LiO_6 octahedron in the spinel-structured Li-rich material, and the incorporation of PO_4^{3-} can result in the average valence of Mn/Ni cations increased to balance more electronegative PO_4^{3-} ions.[46–48] On the other hand, the introduce of large tetrahedral PO_4^{3-} polyanion with high electronegativity into Li-rich cathode is available to restrain local structure distortion in prolonged cycling.[49,50] In addition, the B^{3+} ions doped at tetrahedral sites can block the migration path of TM ions upon electrochemical cycling, thus inhibiting the irreversible phase transition and enhancing the electrochemical stability of Li-rich materials.[51,52]

Based on the comprehensive analysis of XRD, Raman, XPS, and HRTEM images, it has been revealed that one kind of three-in-one nanolayer composed of element-doping, layered-spinel heterostructural transitional connection, and fast ion conductor outer shell was synchronically built onto bulk Li-rich LMNCO particle via a simple surface modification, which could be expected to effectively improve the cycle performance of Li-rich cathode. Series of electrochemical characterizations of the as-synthesized samples were conducted in the voltage range of 2.0–4.8 V. The initial charge-discharge curves of pristine LMNCO and LMNCO@2%LBPO cathodes at 0.1 C (Fig. 3a), exhibit typical profiles of Li-rich cathode, consisting of a sloping curve below 4.5 V and a long plateau around 4.5 V during charging states. Besides, an obvious voltage plateau at ~2.8 V belonged to $Fd\bar{3}m$ spinel structure can be observed in the discharge profile of LMNCO@2%LBPO cathode, which can be confirmed by the cyclic voltammogram (CV) curves with one pair of
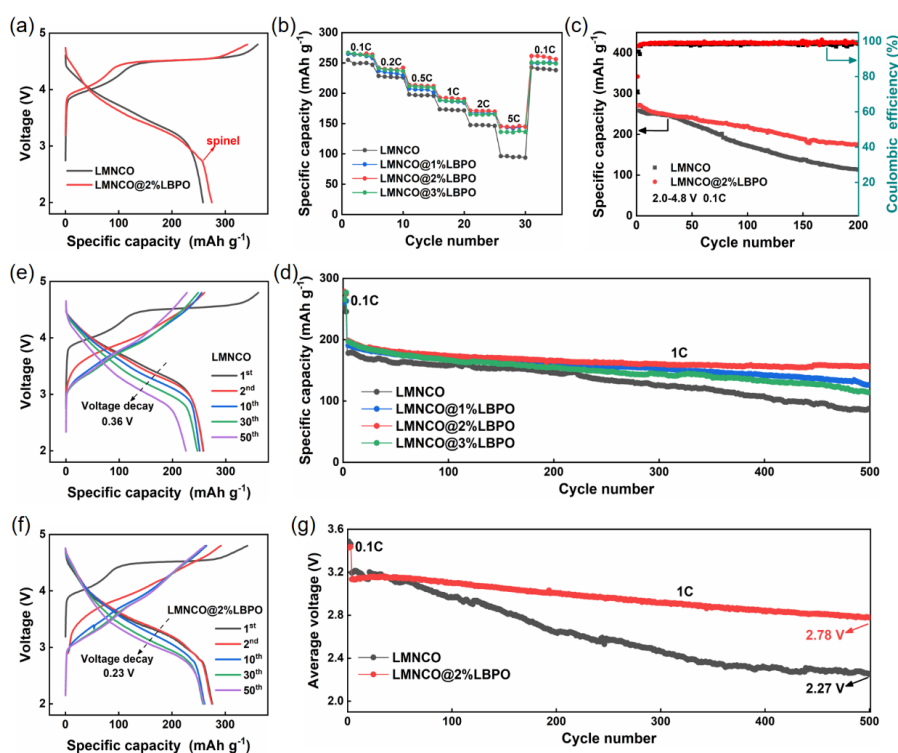

Fig. 3 Electrochemical characterization results of the as-synthesized samples: (a) initial charge/discharge curves of the LMNCO and LMNCO@2%LBPO cathodes; (b) rate performances of all the as-synthesized samples; (c)(d) cycling performance at 0.1 C and 1 C, respectively; (e)(f) voltage-capacity profiles at 1st, 2nd, 10th, 30th, 50th cycle of the pristine LMNCO and LMNCO@2%LBPO cathodes at 0.1 C, respectively; (g) voltage decay profiles of the pristine LMNCO and LMNCO@2%LBPO cathodes at 1 C in the voltage range of 2.0–4.8 V.

oxidation/reduction peaks appeared near 2.90/2.70 V (Fig. S5†).[44] Additionally, all redox peaks of the LMNCO@2%LBPO cathode are well overlapped, better than the pristine LMNCO cathode, directly manifesting the microstructure stability enhanced by LBPO modification. With the improved reversibility of microstructure and redox reactions, the LMNCO@2%LBPO cathode delivers a higher initial discharge capacity of 275 mAh g^{-1}, larger than that of the pristine LMNCO cathode (260 mAh g^{-1}) at 0.1 C under room temperature. The ICE value of LMNCO@2%LBPO cathode is 80.5%, significantly higher than pristine LMNCO cathode (71.5%), confirming the enhanced reversible redox reactions after LBPO modification.

Accordingly, LBPO-modified cathodes have a better rate property than pristine LMNCO cathode (Fig. 3b). At 1 C, LMNCO@2%LBPO cathode delivers a capacity of 192.9 mAh g^{-1}, whereas that of the pristine LMNCO is only 173.5 mAh g^{-1}. Even at 5 C, the discharge capacity of LBPO-modified cathodes can be retained as 145.3 mAh g^{-1}, but that of pristine LMNCO cathode is reduced below 100 mAh g^{-1}. Excellent rate capabilities of LMNCO@LBPO materials should be ascribed to the improved structural stability, three-dimensional Li$^+$ diffusion channels of spinel phase transitional connection and fast ionic conductor LBPO coating shell. Cycling properties of the cathodes were firstly investigated at 0.1 C in the voltage of 2.0–4.8 V, and responding results are shown in Fig. 3c. There is no obvious difference between their specific capacities in the initial several cycles, however the capacity fading of pristine LMNCO cathode is drastic with respect to LMNCO@2%LBPO cathode after 30 cycles. Long-term cycling performances of all the as-synthesized electrodes at high current rate of 1 C have also been demonstrated in Fig. 3d, exhibiting the discharge capacity and cycle stability of LBPO-modified material are both superior to the pristine LMNCO. After 500 cycles, the discharge capacities of LMNCO@1%LBPO, LMNCO@2%LBPO, and LMNCO@3%LBPO cathodes are 125.8, 156.1, and 113.6 mAh g^{-1}, respectively, with the capacity retentions of 65.5% (*vs.* 192.0 mAh g^{-1}), 78.6% (*vs.* 198.5 mAh g^{-1}), and 57.5% (*vs.* 197.4 mAh g^{-1}). In marked contrast, the pristine LMNCO cathode demonstrates an obvious capacity fading from 177.9 to 87.7 mAh g^{-1}, with a lowest capacity retention of 49.3%. The optimized LMNCO@2%LBPO sample can exhibit an outstanding cycling stability even with the current density of 0.2 C under the elevated temperature of 55 °C (Fig. S6†). Comparing Fig. 3e and f, it is obvious that the voltage decay can be significantly suppressed with LBPO modification, since the discharge plateaus of pristine LMNCO cathode are decayed much faster than LMNCO@2%LBPO cathode even at 0.1 C. After 500 cycles at 1 C (Fig. 3g), the discharge voltage plateau of pristine LMNCO cathode is only ~2.27 V, however LMNCO@2%LBPO cathode can display a higher medium voltage of 2.78 V with the small voltage attenuation of 0.73 mV per cycle. The effect of LBPO coating and previously reported modification strategies is further compared in Table S2†, confirming the advantage of LBPO-modified LMNCO cathode material in long-term cycling. These enhanced electrochemical performances and cycling stability of LMNCO@LBPO cathode, should be attributed to the novel surface modification with element doping, spinel phase transitional interface and fast ion conductor coating shell which can effectively stabilize crystalline structure, suppress oxygen loss, and restrain side-reactions at CEI under high current rate and elevated temperature.
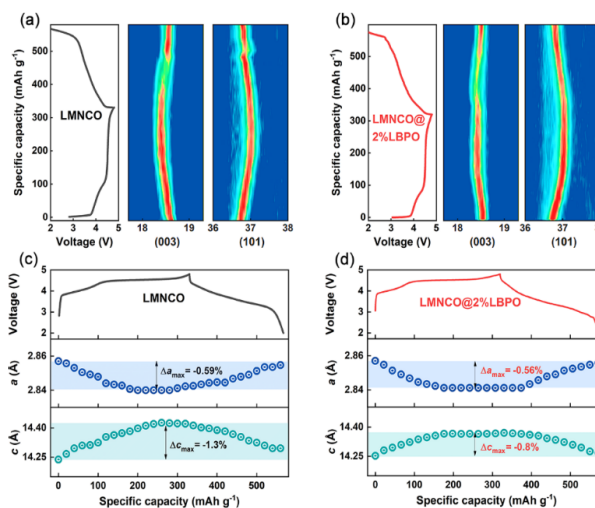

Fig. 4 (a)(b) Color contour mappings of (003) and (101) diffraction peaks and (c)(d) corresponding lattice evolution of the pristine LMNCO and LMNCO@2%LBPO cathodes, respectively, in the initial cycle with voltage range of 2.0–4.8 V.

To explore the detailed crystal structure changes of bulk Li-rich cathodes with/without LBPO coating, in situ XRD technique was employed to investigate them in one delithiation-lithiation cycle, and the lattice parameter evolutions represented by (003) and (101) diffraction peaks are provided in Fig. 4 and Fig. S7.† Upon charging, (003) peaks of pristine LMNCO and LMNCO@2%LBPO cathodes both constantly shift to small angles before 4.5 V, indicating lattice *c*-parameter increased because of Li$^+$ deintercalation from Li-slab and electrostatic repulsive force increased between neighbouring oxygen slabs.[53] At the same time, TM cation oxidations occurred to compensate the charge variation, and lattice *a*-parameter was shrunk because of ionic radii decreased in TM slabs, which is testified by (101) diffraction peak shifting toward high angle.[10] According to the quantitative analysis in Fig. 4c and d, lattice *c*-parameter of pristine LMNCO cathode was increased from 14.23 to 14.43 Å at the end of charge process, while that of LMNCO@2%LBPO cathode changed only from 14.25 to 14.37 Å. The maximum decrease percentages of lattice *a*-parameter in both cathodes are similar (0.59% *vs.* 0.56%), however the maximum increase percentage of *c*-parameter in the pristine LMNCO is 1.3%, obviously larger than that of the LMNCO@2%LBPO (0.8%).

During discharge process, the changes of *a*- and *c*-parameter in both cathodes are analogous because of the inherent delithiation-lithiation mechanism, however it can be observed that the reversibility of *a*- and *c*-parameter in the LMNCO@2%LBPO is superior to the pristine LMNCO cathode. Therefore, it is confirmed that LBPO-modification can stabilize lattice oxygen and strengthen bonding anions with TM cations, as well restrain structure transition, endowing LBPO-modified material with small lattice distortion and volume variation of the host Li-rich framework. Furthermore, ex situ XRD patterns of these two cathodes after 50 cycles at 0.2 C were also collected and further compared with those before cycling (Fig. S8†). It is demonstrated that the peaks between 20° and 22° related with Li$_2$MnO$_3$ superlattice disappeared, along with those shoulder peaks around (104) peak appeared in the 43°–46° range and the ratios of I$_{(003)}$/I$_{(104)}$ lowered.[54] These phenomena suggest that the lattice distortion of host Li-rich framework has both happened in the

pristine LMNCO and the LMNCO@2%LBPO cathodes during repeated cycling. However, the broaden degree of (104) diffraction peak and the decease of $I_{(003)}/I_{(104)}$ intensity ratio are obviously inhibited in the XRD patterns of LMNCO@2%LBPO cathode, partially confirming the improved structural stability of LBPO-modified material.[53]

Crystal structure degradation and phase transition in cycling undoubtedly affect the dynamical properties of Li-rich cathodes, which can be reflected by Li$^+$ kinetics in the electrochemical measurements.[55] CV technique with variable sweep rates was employed to investigate Li$^+$ diffusion in the pristine LMNCO and the LMNCO@2%LBPO cathodes (Fig. 5a and b), and then Li$^+$ diffusion coefficient (D_{Li}) was calculated with the help of following Randles-Sevcik equation,

$$I_p = (2.69 \times 10^5)n^{3/2}C_{Li}Av^{1/2}D_{Li}^{1/2}$$

which shows the linear relationship between current peak (I_p) and the square root of scan rate ($v^{1/2}$), I_p stands for the intensity of oxidation/reduction current peak at specific scanning rate, n represents the number of transferred electrons, C_{Li} is the Li$^+$ molar concentration per unit volume, A represents the contact area between electrode and electrolyte, v is the scanning rate, and D_{Li} denotes the Li$^+$ diffusion coefficient of material.[56] Variable sweep rate CV curves demonstrate that the oxidation/reduction peaks of LMNCO@LBPO cathode are sharper with respect to those of the pristine LMNCO cathode, besides the oxidation/reduction peak of spinel structure invariably displayed at ~2.90/2.70 V. Their fitting lines were also plotted and corresponding slopes are figured out in Fig. 5c and d. It is illustrated that not only during delithiated state but also during lithiated state display the D_{Li} values of LMNCO@2%LBPO cathode visibly larger than the pristine LMNCO, 8.3×10^{-11} vs. 3.7×10^{-11} cm^2 s^{-1} and 4.6×10^{-11} vs. 2.4×10^{-11} cm^2 s^{-1}, respectively. The improved Li$^+$ diffusion of LBPO-modified material provides one rational reason for their better rate performance, which should be contributed to the enhanced structure stability of bulk LMNCO active material, three-dimensional Li$^+$ diffusion channel of spinel-phase transitional connection, and outstanding Li$^+$ conductivity of fast ion conductor LBPO-coating.

Dynamics behaviour of conducting ions in cathode material is influenced by the impedances of battery system, herein electrochemical impedance spectroscopy (EIS) was conducted to investigate the impedance changes of the as-synthesized cathodes at deep delithiated state of 4.8 V.[27] Nyquist plots of the pristine LMNCO and LMNCO@2%LBPO cathodes with different cycles are provided in Fig. 5e and f, additionally the equivalent circuit is fitted to obtain specific values of surface film resistance (R_{sf}) and cathode charge transfer resistance (R_{ct}) listed in Table S3†. The slower increased resistance values of the LMNCO@LBPO cathode, implies its excellent Li$^+$ diffusion in its bulk Li-rich material and at the cathode-electrolyte interface with respect to the pristine LMNCO cathode. Since R_{sf} change is tightly related with the interfacial side reactions between electrolyte and oxygen-activated materials, the smaller values of R_{sf} indicate that the LBPO coating layer can suppress parasitic side reactions at CEI where electrolyte decomposition arises from the attack of carbonate solvents to generate CO, CO$_2$, and H$^+$, leading to the corrosion of HF acid and more nonconductive CEI film formed under high operating voltage.

Morphological characterizations of the cycled pristine LMNCO and LMNCO@2%LBPO electrodes were conducted by SEM technique and
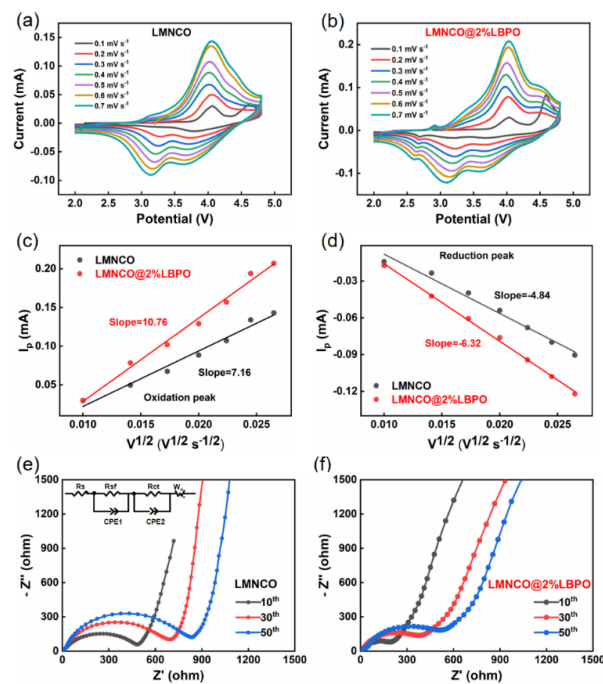

Fig. 5 (a)(b) CV curves with variable sweep rates from 0.1 to 0.7 mV s^{-1} for the pristine LMNCO and LMNCO@2%LBPO cathodes. Linear fitting plots of the current peaks (I_p) vs. square root of scan rates ($v^{1/2}$) for the pristine LMNCO and LMNCO@2%LBPO cathodes: (c) oxidation peaks and (d) reduction peaks, respectively. (e)(f) Nyquist plots with different cycles for the pristine LMNCO and LMNCO@2%LBPO cathodes at high constant voltage charging state of 4.8 V (inset: the equivalent circuit model).

shown in Fig. 6a. Under the same electrochemical treatment, the surface morphology of pristine LMNCO cathode degraded significantly compared with LMNCO@2%LBPO cathode. There more impurities enwrapped outside the pristine LMNCO particles, implies more degradation products generated and R_{sf} value increased, both them are closely correlated with the side reactions at CEI and the TM dissolution from bulk LMNCO electrode during repeated cycling. To confirm the inhibition effect of LBPO coating on TM dissolution from Li-rich cathode, aging experiments were carried out for the pristine LMNCO and LMNCO@2%LBPO materials, subsequently the contents of TM elements were measured by ICP analysis. The quantitative contents of Mn, Ni, and Co elements dissolved into liquid electrolytes have been list in Table S4,† moreover their qualitative comparison is also supplied in Fig. 6b. The contents of TM elements in liquid electrolytes increased with aging time, indicate that the TM dissolution inevitably happened on both cathode materials to some degrees. However, the contents of Mn, Ni, and Co elements dissolved from the LMNCO@2%LBPO are obviously less than those of the pristine LMNCO sample, suggesting the LBPO-modification treatment in this work can effectively suppress the TM dissolution of bulk Li-rich active material during electrochemical cycling. As illustrated in Fig. 6c, the detrimental issues triggered by crystal structure distortion, phase transition and TM dissolution from Li-rich cathode, as well as electrolyte decomposition and HF attack at fragile cathode-electrolyte interface, could be significantly suppressed through constructing three-in-one nanolayer composed of element-doping, layered-spinel heterostructure connection, and fast ion conductor LBPO shell.
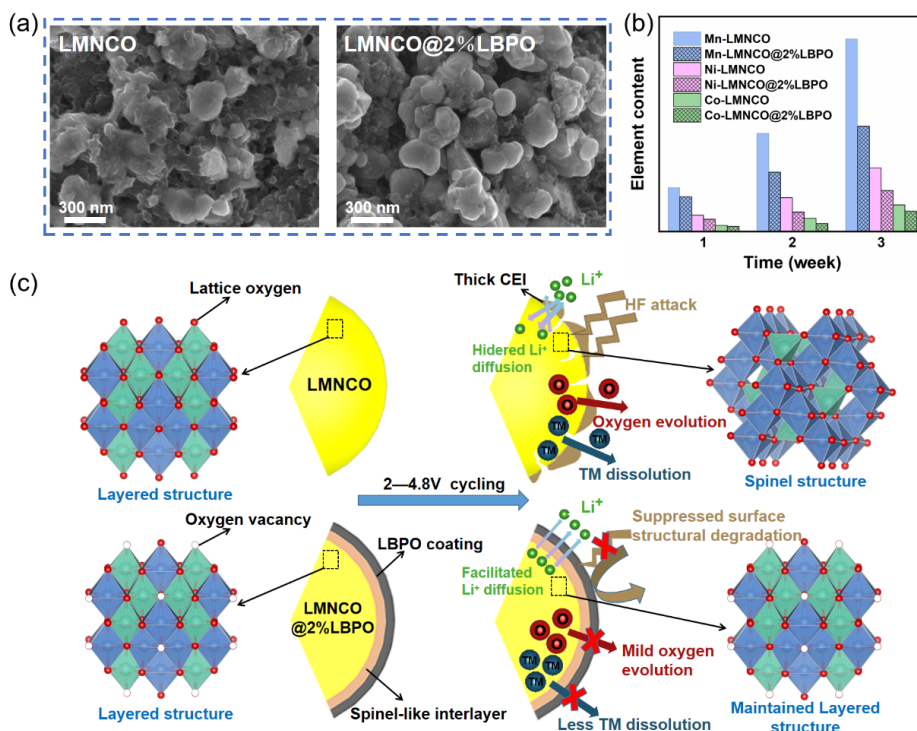
Fig. 6 (a) SEM images of the pristine LMNCO and LMNCO@2%LBPO cathodes before and after 50 cycles at 0.2 C. (b) Content histogram of the transition metal ions (Mn, Ni, and Co) for the LMNCO and LMNCO@2%LBPO samples soaked in liquid electrolytes after 1, 2, and 3 weeks. (c) Schematic diagram of the reaction mechanism at the cathode-electrolyte interface for the pristine LMNCO and LMNCO@2%LBPO cathodes in cycling.

Conclusions

In this study, one novel three-in-one nanolayer was synchronously built onto the LMNCO particles via a facial LBPO-coating treatment. This modification interlayer combining oxygen vacancies and layered-spinel heterostructure together with B^{3+} and PO_4^{3-} polyanion-doping, can stabilize lattice oxygen and prevent oxygen escape from the bulk Li-rich material. In addition, the inherent property of fast ion conductor LBPO coating can effectively facilitate the Li^+ diffusion at CEI and separate bulk Li-rich active cathode from the direct contact with liquid organic electrolyte. In/ex situ XRD, HRTEM, and electrochemical characterizations were employed to investigate the microstructure evolution during Li^+ extraction/insertion, indicating that LBPO coating could prominently alleviate undesired phase transformation, TM dissolution, and the growth of CEI film, which are easily triggered under high operation voltage and elevated temperature. Therefore, the LBPO-modified cathode delivers prominent rate capability and long-term cycle stability together with the well-mitigated voltage decay, *e.g.*, the specific discharge capacity of 150 mAh g^{-1} at 5 C, the capacity retention of 78.6%, and the migrated voltage decay of 0.73 mV per cycle after 500 cycles at 1 C. This work provides one promising modification strategy to obtund the electrolyte corrosion and structure evolution of Mn-based oxide materials in long-term cycling, and promotes the electrochemical performances and the prospective application of Li-rich cathodes in advanced LIBs.

Conflicts of interest

There are no conflicts to declare.

Notes and references

1 B. Li, M. T. Sougrati, G. Rousse, A. V. Morozov, R. Dedryvere, A. Iadecola, A. Senyshyn, L. Zhang, A. M. Abakumov, M. L. Doublet and J. M. Tarascon, *Nat. Chem.*, 2021, **13**, 1070–1080.

2 J. N. Zhang, Q. H. Li, C. Y. Ouyang, X. Q. Yu, M. Y. Ge, X. J. Huang, E. Y. Hu, C. Ma, S. F. Li, R. J. Xiao, W. l. Yang, Y. Chu, Y. Liu, H. G. Yu, X. Q. Yang, X. J. Huang, L. Q. Chen and H. Li, *Nature Energy*, 2019, **4**, 594–603.

3 J. Cao, H. Huang, Y. Qu, W. Tang, Z. Yang and W. Zhang, *Nanoscale*, 2021, **13**, 20488–20497.

Journal Name   **ARTICLE**

4   L. Li, R. Zhao, T. Xu, D. Wang, D. Pan, K. Zhang, C. Yu, X. Lu, G. He and Y. Bai, *Nanoscale*, 2019, **11**, 8967–8977.

5   H. L. Yu, K. B. Ibrahim, P. W. Chi, Y. H. Su, W. T. Chen, S. C. Tseng, M. T. Tang, C. L. Chen, H. Y. Tang, C. W. Pao, K. H. Chen, M. K. Wu and H. L. Wu, *Adv. Funct. Mater.*, 2022, **32**, 2112394.

6   W. He, W. Guo, H. Wu, L. Lin, Q. Liu, X. Han, Q. Xie, P. Liu, H. Zheng, L. Wang, X. Yu and D. L. Peng, *Adv. Mater.*, 2021, **33**, 2005937.

7   C. Yin, X. Wen, L. Wan, Z. Shi, Z. Wei, X. Li, Q. Gu, B. Qiu and Z. Liu, *J. Power Sources*, 2021, **503**, 230048.

8   Y. C. Liu, H. Zhu, H. K. Zhu, Y. Ren, Y. Z. Zhu, Y. l. Huang, L. Dai, S. M. Dou, J. Xu, C. J. Sun, X. L. Wang, Y. Deng, Q. H. Yuan, X. J. Liu, J. W. Wu, Y. N. Chen and Q. Liu, *Adv. Energy Mater.*, 2021, **11**, 2003479.

9   E. Wang, D. D. Xiao, T. H. Wu, X. S. Liu, Y. N. Zhou, B. Y. Wang, T. Lin, X. Zhang and H. J. Yu, *Advanced Funct. Mater.*, 2022, **32**, 2201744.

10 Z. B. Li, Y. W. Li, M. J. Zhang, Z. W. Yin, L. Yin, S. Y. Xu, C. J. Zuo, R. Qi, H. Y. Xue, J. T. Hu, B. Cao, M. H. Chu, W. G. Zhao, Y. Ren, L. Xie, G. X. Ren and F. Pan, *Adv. Energy Mater.*, 2021, **11**, 2101962.

11 J. Ahn, J. M. Kang, M. Cho, H. Park, W. Ko, Y. Lee, H. S. Kim, Y. H. Jung, T. Y. Jeon, H. Kim, W. H. Ryu, J. Hong and J. Kim, *Adv. Energy Mater.*, 2021, **11**, 2102311.

12 J. Liu, Z. Wu, M. Yu, H. Hu, Y. Zhang, K. Zhang, Z. Du, F. Cheng and J. Chen, *Small*, 2022, **18**, 2106337.

13 S. L. Cui, M. Y. Gao, G. R. Li and X. P. Gao, *Adv. Energy Mater.*, 2021, **12**, 2003885.

14 J. M. Kim, X. H. Zhang, J. G. Zhang, A. Manthiram, Y. S. Meng and W. Xu, *Mater. Today*, 2021, **46**, 155–182.

15 H. X. Xie, J. X. Cui, Z. Yao, X. K. Ding, Z. H. Zhang, D. Luo and Z. Lin, *Chem. Eng. J.*, 2022, **427**, 131978.

16 U. Nisar, N. Muralidharan, R. Essehli, R. Amin and I. Belharouak, *Energy Stor. Mater.*, 2021, **38**, 309–328.

17 X. F. Zhang, I. Belharouak, L. Li, Y. Lei, J. W. Elam, A. Nie, X. Q. Chen, R. S. Yassar and R. L. Axelbaum, *Adv. Energy Mater.*, 2013, **3**, 1299–1307.

18 R. B. Yu, Y. B. Lin and Z. G. Huang, *Electrochim. Acta*, 2015, **173**, 515–522.

19 B. Hu, F. Geng, M. Shen, C. Zhao, Q. Qiu, Y. Lin, C. Chen, W. Wen, S. Zheng, X. Hu, C. Li and B. Hu, *J. Power Sources*, 2021, **516**, 230661.

20 Y. Pei, Q. Chen, Y. C. Xiao, L. Liu, C. Y. Xu, L. Zhen, G. Henkelman and G. Cao, *Nano Energy*, 2017, **40**, 566–575.

21 Y. Liu, X. Huang, Q. Q. Qiao, Y. l. Wang, S. h. Ye and X. P. Gao, *Electrochimi. Acta*, 2014, **147**, 696–703.

22 G. Sun, C. T. Zhao, F. D. Yu, R. Z. Yu, J. Wang, J. G. Zhou, G. J. Shao, X. l. Sun and Z. B. Wang, *Nano Energy*, 2021, **79**, 105459.

23 W. Zhu, Z. G. Tai, C. Y. Shu, S. K. Chong, S. W. Guo, L. J. Ji, Y. Z. Chen and Y. N. Liu, *J. Mater. Chem. A*, 2020, **8**, 7991–8001.

24 J. M. Zheng, M. Gu, J. Xiao, B. J. Polzin, P. F. Yan, X. l. Chen, C. M. Wang and J. G. Zhang, *Chem. Mater.*, 2014, **26**, 6320–6327.

25 Q. Xie, Z. Hu, C. Zhao, S. Zhang and K. Liu, *RSC Adv.*, 2015, **5**, 50859–50864.

26 X. Y. Liu, Q. Su, C. C. Zhang, T. Huang and A. S. Yu, *ACS Sustain. Chem. Eng.*, 2015, **4**, 255–263.

27 X. D. Zhang, J. L. Shi, J. Y. Liang, Y. X. Yin, J. N. Zhang, X. Q. Yu and Y. G. Guo, *Adv Mater*, 2018, **30**, 1801751.

28 Q. Y. Li, D. Zhou, L. J. Zhang, D. Ning, Z. H. Chen, Z. J. Xu, R. Gao, X. Z. Liu, D. H. Xie, G. Schumacher and X. F. Liu, *Adv. Funct. Mater.*, 2019, **29**, 1806706.

29 C. Huang, Z. Q. Fang, Z. J. Wang, J. W. Zhao, S. X. Zhao and L. J. Ci, *Nanoscale*, 2021, **13**, 4921–4930.

30 M. Xu, Z. Y. Chen, H. l. Zhu, X. Y. Yan, L. J. Li and Q. F. Zhao, *J. Mater. Chem. A*, 2015, **3**, 13933–13945.

31 S. J. Hu, Y. Li, Y. H. Chen, J. M. Peng, T. F. Zhou, W. K. Pang, C. Didier, V. K. Peterson, H. Q. Wang, Q. Y. Li and Z. P. Guo, *Adv. Energy Mater.*, 2019, **9**, 1901795.

32 R. Zhao, L. Li, T. Xu, D. Wang, D. Pan, G. He, H. Zhao and Y. Bai, *ACS Appl. Mater. Interfaces*, 2019, **11**, 16233–16242.

33 S. Gao, M. Shui, W. D. Zheng, T. C. Yang, J. Shu, L. l. Cheng, L. Feng and Y. l. Ren, *Mater. Res. Bull.*, 2013, **48**, 2896–2900.

34 K. Luo, M. R. Roberts, N. Guerrini, N. Tapia-Ruiz, R. Hao, F. Massel, D. M. Pickup, S. Ramos, Y. S. Liu, J. Guo, A. V. Chadwick, L. C. Duda and P. G. Bruce, *J. Am. Chem. Soc.*, 2016, **138**, 11211–11218.

35 B. Wu, X. K. Yang, X. Jiang, Y. Zhang, H. B. Shu, P. Gao, L. Liu and X. Y. Wang, *Adv. Funct. Mater.*, 2018, **28**, 1803392.

36 P. Liu, H. Zhang, W. He, T. Xiong, Y. Cheng, Q. Xie, Y. Ma, H. Zheng, L. Wang, Z. Z. Zhu, Y. Peng, L. Mai and D. L. Peng, *J. Am. Chem. Soc.*, 2019, **141**, 10876-10882.

37 Z. Ye, B. Zhang, T. Chen, Z. Wu, D. Wang, W. Xiang, Y. Sun, Y. Liu, Y. Liu, J. Zhang, Y. Song and X. Guo, *Angew. Chem. Int. Ed.*, 2021, **60**, 23248–23255.

38 S. H. Li, H. X. Li, H. Y. Zhang, S. Zhang, Y. I. Lai and Z. A. Zhang, *Chem. Eng. J.*, 2022, **427**, 132036.

39 X. Yang, Y. W. Tang, Y. H. Qu, G. Z. Shang, J. Wu, J. F. Zheng, Y. Q. Lai, J. Li and Z. A. Zhang, *J. Power Sources*, 2019, **438**, 226978.

40 S. Jamil, G. Wang, L. Yang, X. Xie, S. Cao, H. Liu, B. B. Chang and X. Y. Wang, *J. Mater. Chem. A*, 2020, **8**, 21306–21316.

41 L. Ku, Y. Cai, Y. Ma, H. Zheng, P. Liu, Z. Qiao, Q. Xie, L. Wang and D.-L. Peng, *Chem. Eng. J.*, 2019, **370**, 499–507.

42 X. H. Zhu, F. Q. Meng, Q. H. Zhang, L. Xue, S. Lan Q. Liu, J. Zhao, Y. H. Zhuang, Q. B. Guo, B. Liu and H. Xia, *Nat. Sustain.* 2021, **4**, 392–401.

43 C. J. Zuo, Z. X. Hu, R. Qi, J. J. Liu, Z. B. Li, J. L. Lu, C. Dong, K. Yang, J. X. Zheng and F. Pan, *Adv. Energy Mater.* 2020, **10**, 2000363.

44 Z. T. Xiao, F. J. Xia, L. H. Xu, X. P. Wang, J. S. Meng, H. Wang, X. Zhang, L. S. Geng, J. S. Wu, and L. Q. Mai, Adv. Funct. Mater. 2022, **32**, 2108244.

45 T. Nakamura, K. Ohta, X. Hou, K. Kimura, K. Tsuruta, Y. Tamenori, R. Aso, H. Yoshida and K. Amezawa, *J. Mater. Chem. A*, 2021, **9**, 3657–3667.

46 Y. Zhao, J. Liu, S. B. Wang, R. Ji, Q. B. Xia, Z. P. Ding, W. F. Wei, Y. Liu, P. Wang and D. G. Ivey, *Adv. Funct. Mater.*, 2016, **26**, 4760–4767.

47 H. Z. Zhang, Q. Q. Qiao, G. Li, R. and X. P. Gao *J. Mater. Chem. A*, **2014**, 7454–7460.

48 H. Liu, B. He, W. Xiang, Y. C. Li, C. Bai, Y. P. Liu, W. Zhou, X. Chen, Y. Liu, S. Gao and X. Guo, *Nanotechnology*, 2020, **31**, 455704.

49 Y. B. Xu, M. X. Zhang, L. Yi and K. Liang, *J. Alloys Compd.*, 2021, **865**, 158899.

50 Y. Liu, D. Ning, L. R. Zheng, Q. H. Zhang, L. Gu, R. Gao, J. C. Zhang, A. Franz, G. Schumacher and X. F. Liu, *J. Power Sources*, 2018, **375**, 1–10.

51 Z. S. Dai, H. L. Zhao, W. X. Chen, Q. Zhang, X. S. Song, G. J. He, Y. Zhao, X. Lu, and Y. Bai, *Adv. Funct. Mater.,* 2022, 2206428.

52 L. C. Pan, Y. G. Xia, B. Qiu, H. Zhao, H. C. Guo, K. Jia, Q. W, X. Gu, and Z. P. Bai, *J. Power Sources*, 2016, **327**, 273–280.

53 K. Chai, J. Zhang, Q. Li, D. Wong, L. Zheng, C. Schulz, M. Bartkowiak, D. Smirnov and X. Liu, *Small*, 2022, **18**, 2201014.

54 B. Jiang, J. R. Li, B. Luo, Q. Z. Yan, H. Li, L. H. Liu, L. H. Chu, Y. F. Li, Q. B. Zhang and M. C. Li, *J.Energy Chem.*, 2021, **60**, 564–571.

55 J. Zheng, M. Gu, J. Xiao, P. Zuo, C. Wang and J. G. Zhang, *Nano Lett.*, 2013, **13**, 3824–3830.

56 Z. Xu, L. Ci, Y. F. Yuan, X. K. Nie, J. W. Li, J. Cheng, Q. Sun, Y. M. Zhang, G. F. Han, G. H. Min and J. Lu, *Nano Energy*, 2020, **75**, 104942.